Research Square

Preprints are preliminary reports that have not undergone peer review.
They should not be considered conclusive, used to inform clinical practice,
or referenced by the media as validated information.

Constraints on magmatic processes and time scales before the Millennium eruption of Changbaishan-Tianchi volcano and their relationship to volcanic unrest

Bingrui Zhou
Institute of Geology, China Earthquake Administration
Fidel Costa
Institut de physique du globe de Paris
Bo Pan
dujushi1981@163.com

Institute of Geology, China Earthquake Administration
Jiandong Xu
Institute of Geology, China Earthquake Administration

Research Article

Keywords: Millennium eruption, Olivine, Diffusion chronometry, Magma intrusion, Earthquakes

Posted Date: November 26th, 2026

DOI: https://doi.org/10.21203/rs.3.rs-11754951/v1

License: This work is licensed under a Creative Commons Attribution 4.0 International License.
Read Full License

Additional Declarations: No competing interests reported.

Constraints on magmatic processes and time scales before the Millennium eruption of Changbaishan-Tianchi volcano and their relationship to volcanic unrest

Bingrui Zhou[1,3](https://orcid.org/0000-0002-5201-6659); Fidel Costa[3]; Bo Pan[1,2,*](https://orcid.org/0000-0003-0998-7369); Jiandong Xu[1,2]

[1]Key Laboratory of Seismic and Volcanic Hazards, Institute of Geology, China Earthquake Administration (IG-CEA), Beijing 100029, China
[2]Jilin Changbaishan Volcano National Observation and Research Station, IG-CEA, Beijing 100029, China
[3]Institut de Physique du Globe de Paris, Université Paris Cité, CNRS, Paris 75005, France

[*]Corresponding author at: Institute of Geology, China Earthquake Administration, Beijing 100029, China.
E-mail address: dujushi1981@163.com

Abstract

The Millennium eruption of Changbaishan-Tianchi volcano, China/DPR.Korea is one of the largest and most explosive eruptions in the past 2000 years. It had a major societal and environmental impact in north-east Asia and beyond. The first phase of the eruption produced comendite magma in November of 946 CE and was followed by a smaller trachyte phase in February of 947 CE. The eruption deposits also contain a range of more mafic compositions found as inclusions with mingling textures in the comendite pumices. Here we report the compositions and textures of olivine crystals found in the deposits with the aim to better understand the processes and time scales involved in the events that led to the eruption. We identified five compositional populations of olivine that could have been in equilibrium with melts ranging from basalt to comendite. Moreover, most olivine crystals show narrow (< 40 μm) Fe-Mg zoning patterns that track several stages of magma interaction, including a progression from mafic-intermediate to mafic-silicic components. Application of diffusion chronometry of Fe-Mg in olivine gives time scales of basaltic magma injection into trachyandesite magma that range from several hours to over 6 years prior to eruption. Further interactions between trachyandesite and trachyte magmas in shallower reservoirs mainly occurred within a month before eruption and illustrates that the entire plumbing system was activated shortly before the eruption. These time scales are within the duration of the recent seismic and geodetic unrest at the volcano in 2002-2005, and agree with monitoring data interpretation of unrest related to magma intrusions and migration. We also investigated the historical written records in China, Korea, and Japan at the time of the eruption and we did not find evidence of seismicity that could be associated with the diking that can be precursors to such a large eruption. Some large tectonic earthquakes were reported half a year to 20 years before the eruption more than 300 km from the volcano. We suggest that the Plinian eruption was probably not triggered by a large earthquake but by the internal dynamics of the system with renewed intrusions and overpressure at various levels.

Key words Millennium eruption; Olivine; Diffusion chronometry; Magma intrusion; Earthquakes

Introduction

Large-scale explosive volcanic eruptions can exert a profound influence on the Earth's climate and have a severe direct impact on the environment and human society (Oppenheimer 2011). Some examples include the 79 CE eruption of Vesuvius, which emitted 4 km^3 dense rock equivalent (DRE) and destroyed the Roman cities of Pompeii and Herculaneum (Sigurdsson et al. 1985; Morgan et al. 2006); the 1883 eruption of Krakatau, Indonesia, which released massive amounts of volcanic gases and triggered devastating tsunami that claimed about 36,000 human lives (Bani et al. 2015); and the 1991 eruption of Pinatubo, Philippines which produced 4-5 km^3 DRE and affected the climate by decreasing global temperature by 0.2°C on average and lasted for 13 months (Boretti 2024). More recently the 2022 eruption of Hunga-Tonga produced large tsunamis that disrupted seafloor ecosystems and damaged >190 km of critical seafloor telecommunication cables (Ribó et al. 2026). Given the severe consequences of these events there are major efforts made to understand the processes and triggers that can lead to such eruptions, and obtain time frames since the beginning of major volcanic unrest to eruptions (Druitt et al. 2012; Newhall et al. 2018; Doronzo et al. 2023; Araya et al. 2024). However, these important questions are difficult to address in a straightforward manner.

The Millennium eruption of Changbaishan-Tianchi volcano is a large Plinian eruption (VEI 6) that consisted of a comendite phase in Nov. 946 CE (~22 km^3 DRE) and followed by a smaller trachyte phase (~2 km^3 DRE) in Feb. 947 CE (Horn and Schmincke 2000; Xu et al. 2013; Oppenheimer et al. 2017; Pan et al. 2020; Yang et al. 2021). The volcanic ash is distributed widely in northeast China, Japan, and also found in Greenland ice cores (Sun et al. 2014; Chen et al. 2016). Though it has been proposed to have

produced a low sulfur emission to the atmosphere, it had a significant climate impact on the regional scale (Xu et al. 2013). Oppenheimer et al. (2017) suggested that the Millennium eruption may also have had profound societal impacts, potentially contributing to the collapse of the Bohai kingdom. Many previous works have been done on this eruption, but there are still limited constraints on the dynamics that lead to this eruption, time scales of magmatic processes, and the potential relationship to volcanic unrest. These topics are the main focus of this contribution.

Previous researches have proposed that the plumbing system of Tianchi volcano consists of magma reservoirs of different physical conditions in multiple crustal levels. The silicic reservoirs of comendite and trachyte may exist within 5 km depth with temperature range 700-900 ℃ (Yi et al. 2021; Wang et al. 2025). The mafic magmas may reside in a wide range of depths, ranging from about 7 to 28 km with magma temperatures higher than 1000 ℃ (Zhang et al. 2018; Guo et al. 2023; Tian et al. 2025; Wang et al. 2025). Previous research on magmatic inclusions and petrological calculations suggest that the redox conditions at this volcano can vary widely. The oxygen fugacity (fO_2) of the silicic magmas as comendite and trachyte ranges between NNO-3 to NNO-2 (Nickel-Nickel Oxide buffer), which is much more reduced than the mafic magma by 3-4 log units (Andreeva et al. 2018; Wang et al. 2025). The water contents of mafic melts are less than 1 wt%, but for comendite melts the water content could be up to 4 wt% (Horn and Schmincke 2000; Iacovino et al. 2016; Andreeva et al. 2019). Several magmatic processes have been proposed as triggers of the Millennium eruption, including injection of deep mafic melts (e.g. trachyandesite and/or basalt) into the silicic reservoirs (Pan et al. 2017; Kuritani et al. 2020; Wang et al. 2025), and mixing of comendite and trachyte (Yi et al. 2021; Chen et al. 2026).

However, the time scales over which these magmatic processes occurred remain poorly constrained. Recent research on the time scales of Tianchi shield-forming basalts (1 to 5 Ma) gives two time scale groups of roughly 10-100 days and 200-800 days by diffusion chronometry (Tian et al. 2025). Other existing geochronological studies have mainly addressed the magma residence times or those relating to long-term magma evolutions. U-Th disequilibrium age of zircon shows 12.2 ± 1.7 ka for comendite and heterogenetic ages 2.6 ± 1.8 ka, 130 ± 10 ka, and >230 ka for trachyte (Zou et al. 2014). Ra/Th age of pre-eruption comendite and trachyte melts are within 6000 and 1600 years respectively, which is shorter than the Ar-Ar age of sanidine (0-19 ka for comendite and 3-10 ka for tarchyte) (Ramos et al. 2016). An even shorter time scale of 100-500 years of sanidine crystallization was given by the Ra/Th method in their subsequent study (Ramos et al. 2019). The time scale involving magma evolution from trachyte to rhyolite is about 10 ka, while 110 ka have been proposed for the evolution from basaltic to silicic magmas (Zou et al. 2008).

Constraining the time scales of pre-eruptive magmatic processes is also important for interpreting volcanic unrest, as magma recharge, migration, and reservoir pressurization may be accompanied by changes in seismicity, ground deformation, and gas emissions (Costa et al. 2020; Costa 2021). Continuous monitoring of Tianchi volcano has been operated for more than 20 years by Changbaishan-Tianchi Volcano Observatory (Pan et al. 2021). The activity status of Tianchi volcano is characterized by the unrest period of 2002-2005, during which the volcano-tectonic earthquakes intensified notably both in frequency and magnitude. This active period was also accompanied by ground inflation and abnormal gas releases, which is considered reflecting some recharge from deep magma and magma reservoir pressurization (Xu et al. 2012; Liu et al. 2026). Though there is limited knowledge on any historical unrest associated with the Millennium eruption.

Here, we investigate olivine crystals found in the deposits of the Millennium eruption, focusing on their chemical compositions and zoning patterns. We applied thermodynamic modeling to constrain the physical conditions of the magma reservoirs and diffusion chronometry to quantify the time scales recorded by the chemical zoning in olivine. These results were integrated to reconstruct the dynamic plumbing system prior to the eruption. Furthermore, we compare the diffusion-derived time scales to recent seismic unrest and historical earthquake accounts to explore the potential links between geophysical unrest signals and magmatic processes at Tianchi volcano.

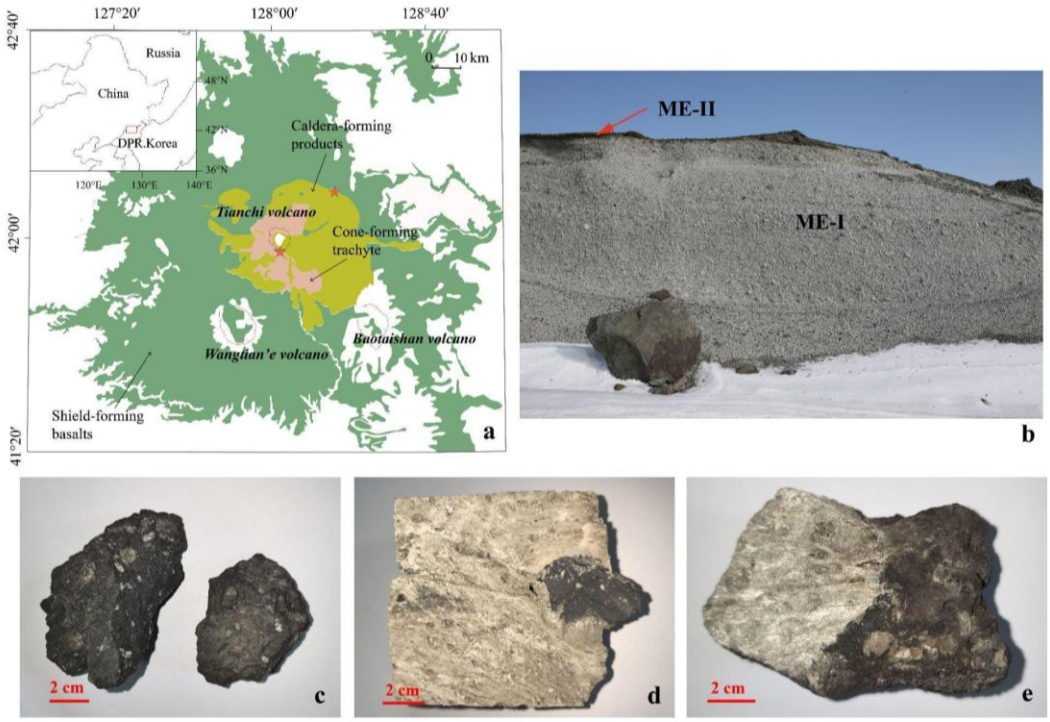


Fig. 1 Geological map of Changbaishan-Tianchi volcano and hand specimens of the studied samples. (a) Location of Changbaishan-Tianchi volcano (Red stars show the sampling points). (b) Field picture of the deposit of the Millennium eruption (about 3 meters thick). (c) Trachyandesite block fragments found in ME-I comendite (NTA sample labels). (d) Trachyandesite enclave in ME-I comendite pumice (MAC sample labels). (e) ME-II trachyte mingled with ME-I comendite (MTC1 sample labels) found in ME-I deposit.

Field relation and samples

The Millennium eruption consisted of two events: the first one (ME-I in Fig. 1b) occurred on Nov. 3, 946 CE, and formed a thick deposit of white pumice of comenditic composition; and the second one (ME-II in Fig. 1b) occurred about three months later on Feb. 7, 947 CE, and formed a relatively thin black pumice layer of trachytic composition right over ME-I (Xu et al. 2013; Oppenheimer et al. 2017; Pan et al. 2017, 2020). Comendite and trachyte pumices can be found as mingled hand specimen samples in the deposit (Fig. 1e). In addition to the comenditic and trachytic magma types, trachyandesitic dark blocks are found scattered in the white pumice deposit and in the pyroclastic flow of ME-I. These blocks appear as small lava fragments (Fig. 1c) or as enclaves surrounded by comendite pumice (Fig. 1d).

We focused our work on samples of the ME-I deposit (Table 1) as they likely contain the most relevant information to constraint the processes that occurred right before the beginning of the eruption and which could be related to its trigger. The samples include: (1) black blocks of trachyandesite (samples labelled NTA1 and NTA2), (2) mingled blocks of trachyandesite and comendite (samples MAC1 and MAC3), (3) mingled blocks of trachyandesite, comendite, and trachyte (MAC2), and (4) Mingled samples of trachyte and comendite (MTC1). We made petrographic thin sections of unaltered samples. For the heterogeneous samples, we made thin sections at the contact/margins between the enclaves and host or along the mingled zones of the two magmas.

Table 1 Sample list and description

Eruption	Sample labels	Sample Locations	Description	Number of Olivine crystals in thin sections
ME-I (Nov. 3 946 CE)	NTA1	In comendite pumice deposits on the south summit of Tianchi	Trachyandesite lava blocks (5-8 cm diameter)	24
	NTA2	In comendite pumice deposits on the south summit of Tianchi	Trachyandesite lava blocks (5-8cm diameter)	37
	MAC1	In pyroclastic flow on the south slope of Tianchi	Comendite pumice with trachyandesite enclave	5

MAC2	In pyroclastic flow on the south slope of Tianchi	Comendite pumice with trachyandesite enclave, plus pumice fragments of trachyte	8
MAC3	In pyroclastic flow near Dongfanghong bridge, northeast slope	Comendite pumice with trachyandesite enclave	6
MTC1	In pyroclastic flow on south slope of Tianchi	Mingled sample of trachyte pumice and comendite pumice	5

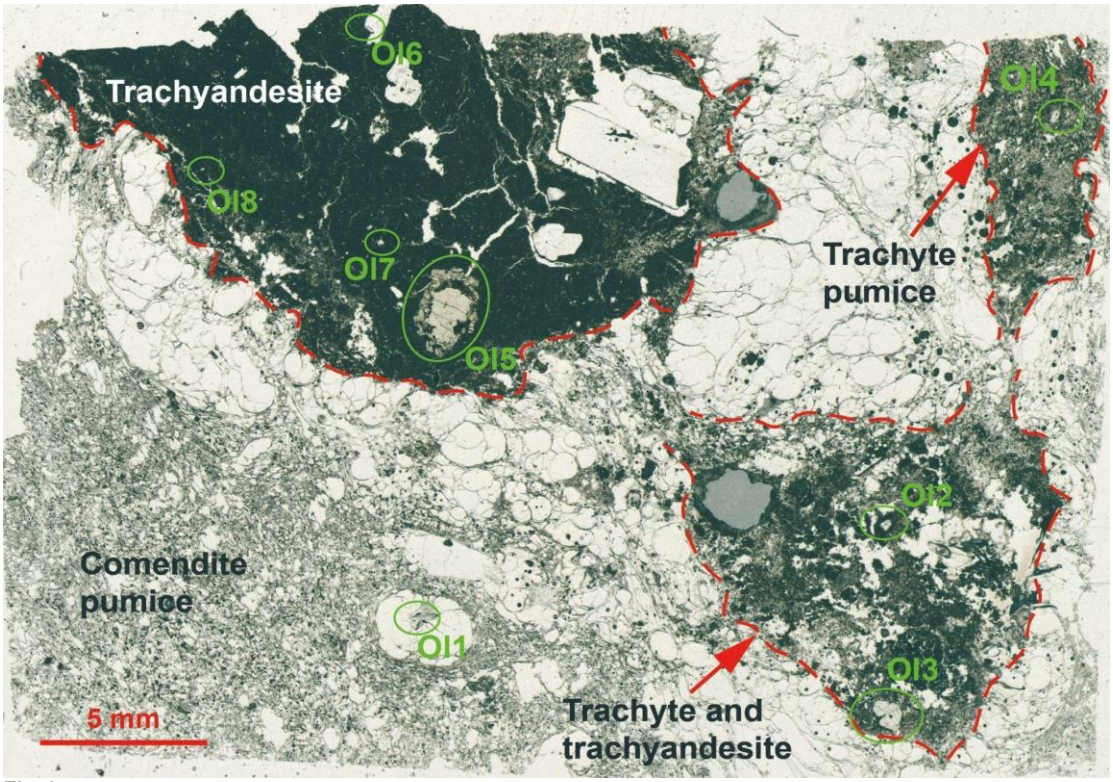


Fig. 2 Full section image of MAC2 sample that consists of the comenditic pumice host and trachyandesite enclave, trachyte pumice fragments, and apparently mingled zone of trachyandesite and trachyte. The green circles show the locations of the olivine crystals we have studied.

Methods and strategy

1 Analytical methods

We observed the thin rock sections under the optical microscope, and made scanning petrographic pictures of the entire thin sections. We identified 85 olivine crystals in total and labeled each of them (Fig. 2 and Supplementary). The crystallinity of the samples was obtained using the point counting method with the open-access software JmicroVision.

The thin sections were then observed by a ZEISS EVO MA-10 Scanning Electron Microscope (SEM) in the Institut de Physique du Globe de Paris (IPGP). We obtained 75 Back Scattered Electron (BSE) images using a voltage of 15 kV and searched for compositional gradients in olivine crystals seen as grey scale changes.

We selected 35 olivine crystals with the most apparent zoning features to conduct Electron Probe Micro-Analyzer (EPMA) by a CAMECA SX-Five equipment in OSU Ecce Terra, Sorbonne Université. The calibration procedure was conducted by analyzing a minimum 3 points for each standard sample (Albite, Garnet, Orthoclase, Olivine, Cr_2O_3, NiO). The analyzing condition of our olivine samples was set to 15 kV and 10 nA for element Mg, Fe, Si, while 15 kV and 160 nA for element Ni, Mn, Al, Zn, Ca. The beam size was set to 1 μm which is the minimum of the instrument. The analysis traverses were taken from crystal-glass margin towards the interior of each olivine crystal. The distance between each analysis point is generally between 1 μm and 2 μm. In total we made 47 traverses which make up about 1872 of individual analysis. The analytical precision is reported as relative error (2σ) which is about 1% for Mg, Fe, Si, and 0.05% for Ni, Mn, Al, Zn, Ca. After analysis we calculated the structural formula of olivine using 4 oxygen criteria. We only kept those analyses with oxide totals between 98 wt% and 102

wt%, and with <0.1 wt% Al_2O_3 content and with total cations per formula unit (Σapfu) between 2.97-3.03. As the zoning profiles are short, our main concerns were to avoid mixed analysis between the matrix glass and the crystal rims. We then calculated the forsterite (Fo) composition of the olivine as 100Mg/(Mg+Fe) in moles.

The orientation of the crystallographic axis of olivine crystals was obtained by an Oxford-Nordlys Nano electron backscatter diffraction (EBSD) system integrated to the Zeiss-sigma SEM at Institute of Geology, China Earthquake Administration (IG-CEA). The acceleration voltage was set to 20 kV. Euler angles derived by EBSD analysis were converted to trend and plunge angles through the orientation matrix. The angles between the crystallographic axis and EPMA traverses (α, β, and γ) were then calculated and projected using the Stereo32 software developed at Ruhr-Universität Bochum.

2 Thermodynamic modelling methods

The olivine compositions are controlled by the composition of their coexisting melt compositions as well as the intensive parameters such as temperature (T), pressure (P), and oxygen fugacity (fO_2). We applied the thermodynamic MELTS modeling (Ghiorso and Sack 1995; Gualda et al. 2012) to reproduce the olivine compositions in our samples (Kahl et al. 2015; Giuffrida and Viccaro 2017). The starting melt compositions used in the modeling are representative of magmas from Tianchi volcano and we aimed at reproducing the measured olivine compositions, except for the most Fe-rich one that grew from the comendite, which we have not attempted to reproduce (Wang et al. 2025). We used the trachyandesite sample NTA1 and the basalt sample JJ-5 (Tab. 2). For NTA1 is the most mafic rock in our sample which has a Mg# of 46.4 [100Mg/(Mg+0.85Fe) mol%] assuming redox condition around NNO to QFM, and the basalt sample JJ-5 is from Pan et al. (2020).

Table 2 Initial compositions used in MELTS modeling

Oxide in wt%	**JJ-5**	**NTA1**
	Basalt	Trachyandesite
SiO_2	51.7	57.72
TiO_2	2.47	1.66
Al_2O_3	15.37	16.38
FeO_T	10.74	7.03
MnO	0.15	0.1
MgO	5.86	2.9
CaO	8.43	5.92
Na_2O	3.23	4.56
K_2O	1.49	3.27
P_2O_5	0.43	0.37
Total	99.87	100
Mg#	53.3	46.4

We explored a range of Pressure-Temperature and water content in the melt, and oxygen fugacity guided by results from previous studies. The water content was varied between 0.1 wt% to 5 wt%, which covers the previous results of hygrometer and melt inclusions (Andreeva et al. 2019; Wang et al. 2025; Yeo et al. 2026). The modeling temperature ranges from the liquidus temperature of the initial bulk rock to 850 ℃, which is related to trachytic magma in Tianchi volcano (Wang et al. 2025). We conducted the modeling under NNO, QFM, and QFM-1 constraints respectively, considering the fO_2 of Tianchi volcano varies from NNO for mafic magma and more reduced environment for evolved magmas (Andreeva et al. 2018; Wang et al. 2025). The total pressure was varied between 0.5-4 kbar that covers the depth of Tianchi crustal magma reservoirs (Zhang et al. 2018; Yi et al. 2021; Wang et al. 2025).

More than 300 modeling runs were conducted following the strategy that the initial composition equilibrates in any H_2O-pressure combinations along a set oxygen fugacity buffer, and the crystallized olivine crystals are recorded by their forsterite compositions and crystallizing temperatures (Fig. 6). Theoretically, the olivine crystals of observed Fo compositions could only be reproduced in a certain set of P-T-fO_2-H_2O, thus giving us first-order constraints to the physical conditions of our samples.

3 Diffusion chronometry methods

The compositional zoning in Fo can be modelled as Fe-Mg inter-diffusion after abrupt environmental change caused by any given magmatic process (Costa et al. 2008). This re-equilibration via diffusion can be described by Fick's second law (in one dimension):

$$\frac{\partial C_i(x,t)}{\partial t} = \frac{\partial}{\partial x}\left(D_i \frac{\partial C_i(x,t)}{\partial x}\right) \quad (1)$$

where C_i is concentration of elements (in this case Fo), x is distance from crystal rim to interior, t is time of diffusion, and D_i is compositional dependent diffusion coefficient. The main idea of the modelling is that we calculate $C_i(x,t)$ at discretized x and t domains from an initial Fo profile. Time t could be obtained when our calculated $C_i(x,t)$ fit the natural Fo profile by minimum the root mean square. The numerical solution of diffusion equation (Eq. 1) follows the one-dimensional finite-difference scheme described in Costa et al. (2008) which was solved using Python codes that were developed for this work.

The choice of the initial and boundary conditions was guided by the shapes of the observed Fo zoning patterns. A homogenous initial profile was suitable for both normally and reversely zoned olivine, because the observed compositional plateaux near the core of these crystals preserved the feature that was not affected by diffusion (Fig. 4b and d). A step-function initial was applied in some cases where a small plateau shows at the crystal rim. For the olivine with complex zoning features (e.g. Ol8-MAC2 in Fig. 4), we considered a two-stage modeling scheme, where the initial condition of the second stage was the diffused profile of the first stage modeling (Kahl et al. 2011). This scheme could simulate two successive magmatic events, thus the results involve two time scales that we defined as Δt_1 and Δt_2 (separating from those time scales from single modeling profiles). As for the boundary condition between the crystal surface and melt, we used a fixed concentration based on the scenario that the boundary is open to Fe-Mg transferring and an infinite volume of the magma reservoir compared to the mineral (Costa et al. 2008).

Diffusion coefficient D (m^2/s) of Fo is expressed as follows (Dohmen and Chakraborty 2007; Dohmen et al. 2007):

$$D_{Fo} = 10^{-9.21} \cdot \left(\frac{fO_2}{10^{-7}}\right)^{1/6} \cdot 10^{3(X_{Fe}-0.1)} \cdot exp\left(-\frac{201000+(P-10^5)\cdot 7\cdot 10^{-6}}{RT}\right) \quad (2)$$

where T is temperature in Kelvin, P is pressure in Pascals, fO_2 is oxygen fugacity also in Pascals, X_{Fe} is the mole fraction of the fayalite component, and R is the gas constant in J/(mol*K). Considering the strong anisotropy of diffusion of Fe-Mg in the olivine crystals, the diffusivity along the EPMA traverses were calculated by (Costa and Chakraborty 2004):

$$D_i = D_{i,[100]} \cdot cos^2\alpha + D_{i,[010]} \cdot cos^2\beta + D_{i,[001]} \cdot cos^2\gamma \quad (3)$$

where $D_{i,[100]}$ refers to the diffusivity of component i along the crystallographic axis [100], analogously for $D_{i,[010]}$ and $D_{i,[001]}$. α, β, and γ are angles between the crystallographic axis [100], [010], [001] and EPMA traverses.

The diffusion coefficient is a function of physical conditions T, P, and fO_2, which is constrained by our MELTS modelling, geothermometry, and previous results. As we describe in detail in result sections, a temperature of 1059 ± 29 °C was used in modeling the interactions occurring in the M_1 reservoir (the median value from the olivine-liquid geothermometry). The pressure (1.5 kbar) and fO_2 (NNO) are given from MELTS constraints of modeling the trachyandesite NTA1. Similarly, the T, P and fO_2 conditions for interactions involving M_0, M_1, M_2 that point to the mm_1 environment were constrained by the MELTS modeling of mm_1 reservoir (1005 ± 99 °C for temperature, 1.5 kbar for pressure, and QFM buffer for fO_2). The detailed conditions used in the modelling are further described in the following sections and summarized in Supplementary Table S1.

The uncertainties of the time estimation may arise from many aspects such as sectioning effect, anisotropic diffusion, and intensive parameters, etc. (Costa et al. 2008, 2020; Shea et al. 2015). Here we evaluated the uncertainties related to the temperature input and the analytical precision of the micro-probe data following the method described by (Girona and Costa 2013):

$$\sigma(t) = \begin{cases} +\{(n+1)\Delta t + t[exp\left[\tau\left(\frac{1}{T} - \frac{1}{T-\sigma(T)}\right)\right] - 1]\} \\ -\{(m+1)\Delta t + t[1 - exp\left[\tau\left(\frac{1}{T} - \frac{1}{T+\sigma(T)}\right)\right]]\} \end{cases} \quad (4)$$

The asymmetric time uncertainty σ *(t)* consists of two terms: (1) the time difference related to the modeling profiles that yield longer or shorter times than the best fit profile but same in discrepancy, where *m* and *n* are the numbers of such profiles. The discrepancy refers to the numbers that the modeled profile mismatch by falling out of the error bars of the natural profiles. The sizes of error bars are absolute errors on Fo (2σ) that we transmitted from independent uncertainties of MgO and FeO; (2) the uncertainty propagated from temperature difference σ *(T)* through the diffusion coefficient equation (Eq. 2), where τ is the exponential term involving activation energy, pressure, and gas constant. We took the value of σ *(T)* from the temperature range of thermodynamic modeling or the model error of the geothermometry (Putirka 2008).

RESULTS

1 Petrological observations

The trachyandesite samples (NTA1, NTA2) exhibit porphyritic textures, with about 15 vol% of phenocrysts (crystals >300 μm in diameter) consisting of plagioclase, olivine, pyroxene and Fe-Ti oxides. Some plagioclase phenocrysts show compositional zoning and sieve textures with resorption surfaces. The groundmass is predominantly composed of plagioclase microlites and abundant vesicles (Supplementary Fig. S1 and S2).

MAC1 and MAC3 are heterogeneous samples made of trachyandesite and comendite, with a clear boundary between them (Supplementary Fig. S3 and S4). The trachyandesite occurs as enclaves and it is texturally similar to the NTA samples. The comendite host is a white/gray pumice, characterized by low phenocryst contents that include sanidine, quartz, rare olivine and Fe-Ti oxides. The samples are highly vesiculated. Wang et al. (2025) also reported such samples but the enclaves were described as trachybasalts. The heterogeneous sample MAC2 is more complex, it contains irregular fragments of trachyte in addition to trachyandesite. These trachytic pumices appear to form hybridized zones with the trachyandesite (Fig. 2).

MTC1 is a mingled sample made of a comendite and trachyte part (similar to the mingled trachyte-comendite clast in Pan et al. (2017). The sample consists of two distinct pumice textures (Supplementary Fig. S5). The comendite part contains few feldspar phenocrysts with dissolution textures and elongated vesicles with thin bubble walls, whereas the trachyte part contains a higher crystal content, mainly composed of feldspar and olivine.

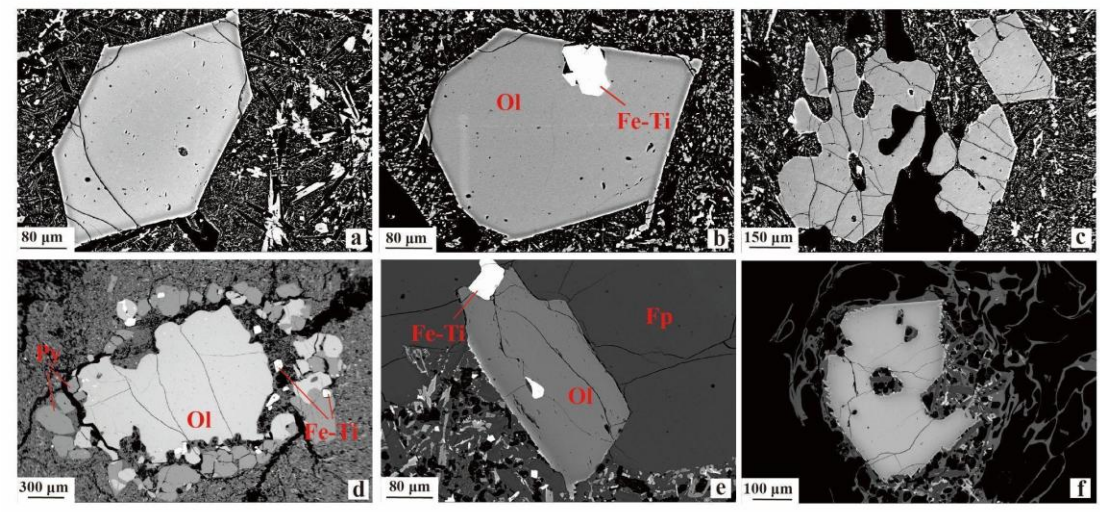


Fig. 3 Representative BSE images of olivine crystals. **a** Euhedral and zoned olivine (Ol4) in trachyandesite sample NTA1. **b** Subhedral zoned olivine (Ol25) with Fe-Ti oxide inclusion in trachyandesite sample NTA1. **c** Anhedral olivine (Ol10) in trachyandesite sample NTA1. **d** Olivine crystal (Ol5) that shows resorption features and reaction rim made of pyroxene and Fe-Ti oxide in trachyandesite enclave of mingled comendite sample MAC2. **e** Anhedral olivine (Ol6) partly included in feldspar in mingled comendite sample MAC2. **f** Anhedral olivine (Ol1) that is zoned and surrounded by the trachyte groundmass in mingled sample MTC1.

2 Olivine textures and composition

Olivine phenocrysts in the trachyandesite samples (NTA1, NTA2) are commonly euhedral to subhedral, although some may be skeletal and show resorption/embayment textures (Fig. 3a, b, and c). Olivine crystals in mingled comendite samples (MAC1, MAC3) are found as large euhedral phenocrysts (>300

μm) and relatively small anhedral crystals (<100 μm). We found only one crystal (Ol5) in a comendite pumice from mingled comendite MAC1, all the other olivine crystals are found in the trachyandesite enclaves. Olivine crystals in the mingled comendite MAC2 sample are also mainly found in the trachyandesite enclave or mingled part of trachyandesite and trachyte. They vary in size from >1 mm to <100 μm with subhedral or anhedral shapes. Some olivine is found surrounded by feldspar or by a reaction rim of small olivine, pyroxene, and Fe-Ti oxides (Fig. 3d and e). In the mingled trachyte and comendite sample MTC1, olivine is only found in the trachyte pumice. The crystals are generally small (<300 μm) and anhedral, and resorption and embayments are common (Fig. 3f). From BSE images, it is apparent that most olivine crystals show an almost homogeneous interior in greyscale that makes most of the crystal and show a darker or brighter greyscale closer to the crystal margin, implying higher Mg or Fe concentrations towards the rims. These chemically zoned olivine crystals to our knowledge have not yet been reported in the Millennium eruption.

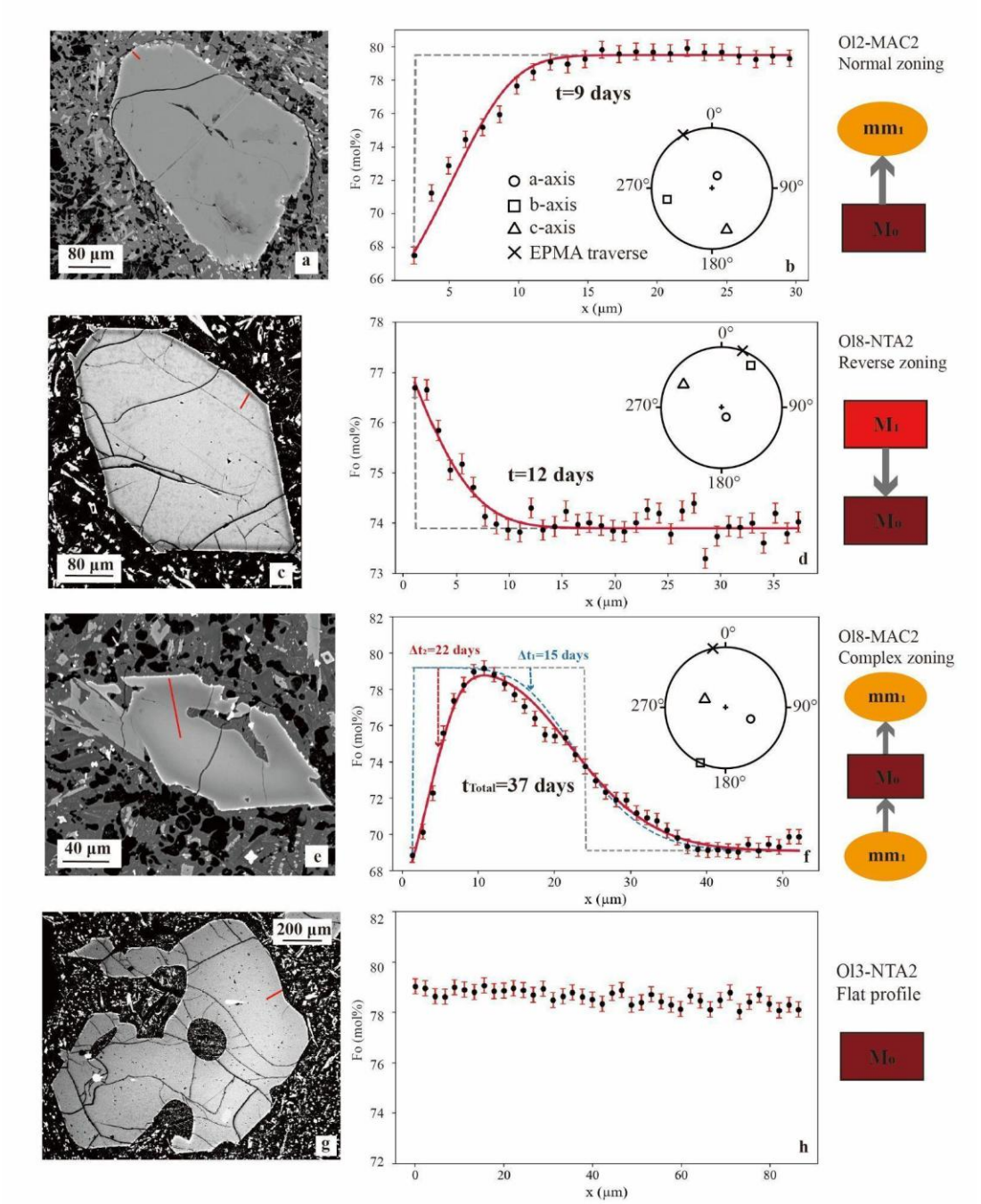


Fig. 4 Representative olivine crystals, zoning profiles, diffusion models and schematic environments. **a, b** Normal zoning. **c, d** Reverse zoning. **e, f** Complex zoning. **g, h** Homogeneous profile. EPMA traverses were labeled on the BSE images as red lines and their orientation relations with crystallographic axes were shown as insets in b, d, and f as lower hemisphere projection. For the diffusion modeling profiles in b, d, and f, data points with error bars are measured Fo profiles, while the red lines are the best

fit profiles of diffusion modeling. The initial conditions are shown as dashed lines. On the right most panel shows the proposed sequence of events associated with each olivine crystal.

The olivine crystals of the ME-I eruption show a large range of Fo content [Fo=100Mg/(Mg+Fe), in mol%] from 2.6 to about 80. Most olivine crystals display very short Fo zoning (about 20 to 40 μm) from the crystal margins towards their interiors, except for a few crystals with zoning lengths between 50 and 200 μm, and some crystals that are virtually unzoned (or zoning of less than about 3 μm). We classified the zoning patterns into 4 different types: (1) normal zoning: Fo content decreases from the crystal interior towards the margin (Fig. 4a and b); (2) reverse zoning where Fo content increase from crystal interior towards its margins (Fig. 4c and d); (3) complex zoning where Fo content first increases and then decreases from the interior towards the margin (Fig. 4e and f); and (4) homogenous olivine with with no apparent Fo zoning from the interior to the margin (Fig. 4g and h).

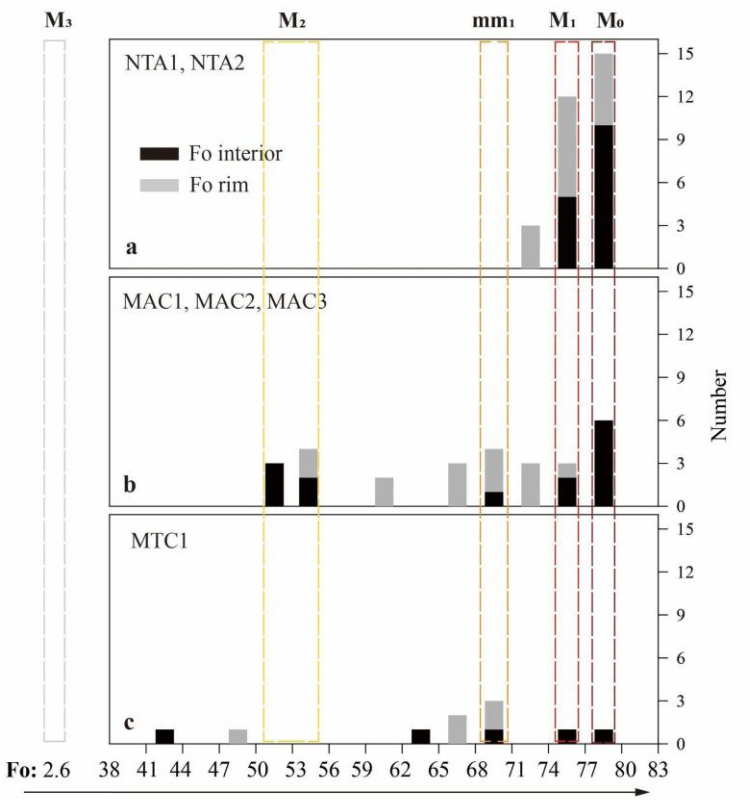


Fig. 5 Histogram of olivine interior and rim composition organized by samples: Trachyandesite (NTA1 and NTA2), mingled samples with trachyandesite (MAC1, MAC2, and MAC3), and mingled trachytic and comenditic pumice (MTC1). The vertical dashed lines mark the proposed magmatic environments M_0, M_1, mm_1, M_2, M_3 according to the different compositional plateaux of the olivine groups. Group M_3 is represented by a single olivine of very low Fo in the sample MAC1.

3 Magmatic environments

Most of the olivine crystals we have analyzed consist of a Fo homogeneous plateau in their interiors and short zoning (typically < 50 μm) towards rims. We interpret this to mean that the olivine crystals grew in a relatively stable magma environment that allows olivine crystals to have a nearly constant core composition (Kahl et al. 2011, 2015). Then with changing of physical conditions in magma environments (temperature, pressure, composition of the melt, fO_2, etc.), the olivine changed its composition to equilibrate the new surrounding environments. Any open-system interactions between magma reservoirs or magma processes such as intrusion or mixing could result in these changes.

Following the concept discussed in Kahl et al. (2011) and subsequent publications (e.g. Giuffrida and Viccaro 2017; Pelullo et al. 2022; Romano et al. 2026), we assume that well defined magma environments can be proposed by a distinct olivine core homogenous composition (Fig. 5). We have identified two magma environments of high Fo olivine groups (M_0: Fo78-80; M_1: Fo74-76), which are found in all samples. These olivine compositions are also common in much older Changbaishan basaltic eruptions (Tian et al. 2025). We propose an additional M_2 magma environment which is represented by a lower Fo50-55 population, and only found in mingled samples MAC1, MAC2 and MAC3. We also identified a magma environment M_3 as recorded by a very Fe-rich crystal (Fo2.6). Though we only find 1 such crystal in our samples (in comendite pumice of MAC1), this type of olivine is well reported in

other publications where they are commonly found in comendite (Wang et al. 2025; Chen et al. 2026). Moreover, we also propose an intermediate magma environment as mm_1 (Fo68-71). This environment may not represent a distinct magma reservoir for it contains less population in terms of olivine interiors. It can be understood as a temporary environment formed by mixing between different magmas such as M_0(or M_1) and M_2 and is also recorded by the many rim compositions (see discussion below).

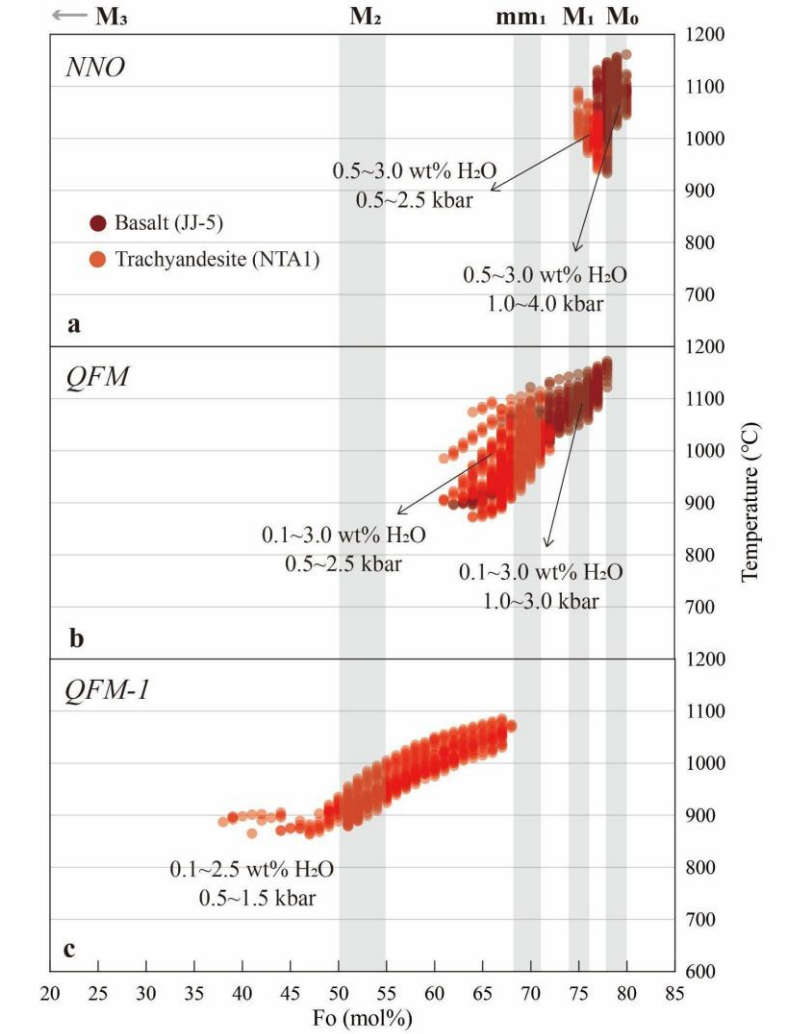


Fig. 6 MELTS modeling (Ghiorso and Sack 1995; Gualda et al. 2012): olivine Fo versus equilibrium temperatures for a range of fO_2, P and water content in the melt. The modelled olivine compositions are projected together with the magma environments M_0, M_1, M_2, mm_1, and M_3. The initial compositions of modelling are bulk rock composition of a basalt sample JJ-5 (Pan et al. 2020) and a trachyandesite sample NTA1. The upper, middle, and lower panels (a, b, and c) are models along NNO, QFM, and QFM-1 fO_2 buffers, in which the pressure and H_2O contents vary within the marked ranges.

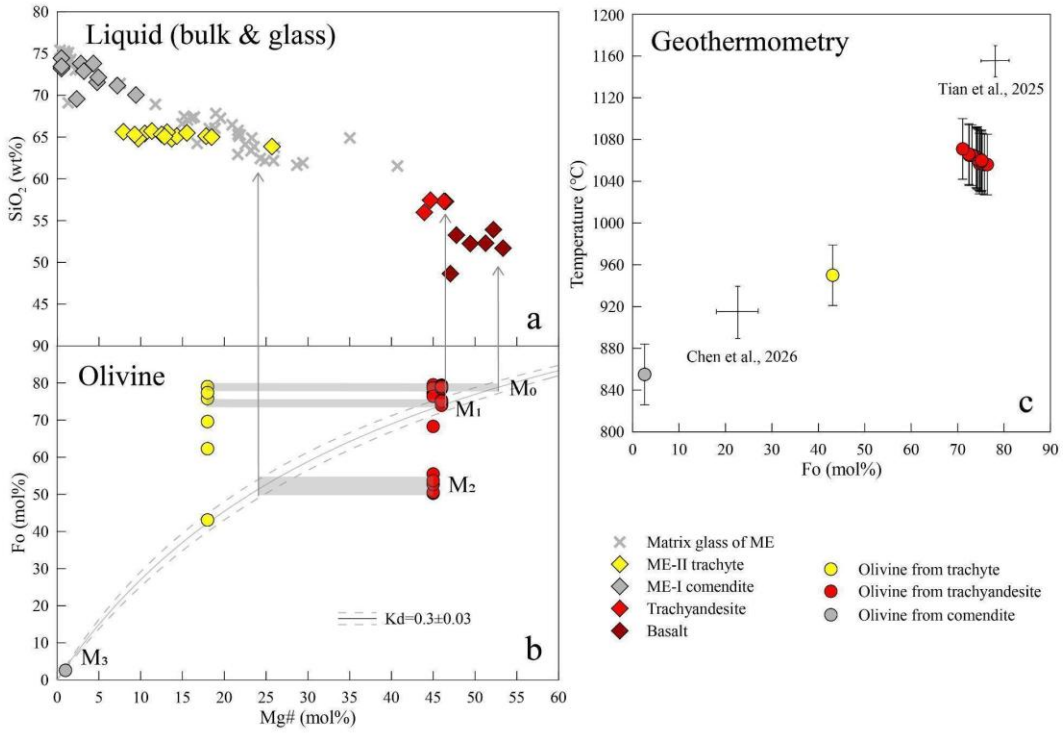


Fig. 7 Olivine-liquid equilibrium and geothermometry diagram. **a** Mg# vs. SiO_2 diagram of liquid compositions of magmas. **b** Equilibrium tests of olivine and their hosting melts. **c** Temperature results of geothermometry vs. olivine Fo. Data sources in **a** are from Pan et al. (2017, 2020). The Fe-Mg exchange coefficient Kd in **b** follows Roeder and Emslie (1970). The Fo values are from the core compositions of each olivine. The temperature results in **c** are calculated from the olivine-liquid geothermometry (Putirka 2008) only when Kd=0.3±0.03. Results of olivine temperature from previous studies were also presented as crosses (Tian et al. 2025; Chen et al. 2026).

4 Physical conditions of magma environments

Combining the petrological observations and the MELTS modelling we propose the following magmatic environments and conditions.

M_0 (Fo78-80): The olivine of this environment crystallized from basalt composition JJ-5 under the NNO buffer, within a pressure range 1 to 4 kbar (Fig. 6a). The H_2O contents in the melt range 0.5 to 3 wt%. The crystallizing temperature of M_0 olivine ranges from 1049 ℃ to 1161 ℃ depending on the H_2O. Our T-P range of M_0 olivine overlaps with those calculated from pyroxene in the mafic magma (Wang et al. 2025). Though our pressure range is relatively lower than those calculated from basalt units of 6-9 kbar (Guo et al. 2023). We further found that M_0 olivine is not in equilibrium with its host trachyandesite, but in equilibrium with the JJ-5 basalt (Fig. 7a and b).

M_1 (Fo74-76): M_1 olivine could crystallize from the trachyandesite (NTA1) under NNO buffer and P<2.5 kbar (Fig. 6a). The crystallization temperature of M_1 olivine is 891-1091 ℃ given the large possible variation of H_2O content in the melts (0.5 to 5.0 wt%). These M_1 olivine crystals are in equilibrium with their host magma trachyandesite (Fig. 7a and b), thus an independent calculation of 1056 to 1063 ℃ was given by the olivine-liquid geothermometry (Putirka 2008). Though there is no direct H_2O estimation of trachyandesite from previous works, we consider that the H_2O content should be lower than the maximum H_2O content of 3 wt% which is calculated by Ca in olivine geohygrometer (Yeo et al. 2026). Therefore, the MELTS modeling gives a temperature constraint within 960-1091 ℃, which is overlapping with the results of the olivine-liquild geothermometry.

mm_1 (Fo68-71): Olivine of intermediate magma mm_1 can be generated from trachyandesite NTA1 or basalt JJ-5 under QFM buffer with pressure range in 1-2.5 kbar (Fig. 6b). The crystallization temperature from MELTS ranges 906 to 1105 ℃ when H_2O varies from 0.1-3.0 wt%. Our temperature overlaps the previous results of basalts but tends to be cooler by about 70 ℃ (Zhang et al. 2018; Guo et al. 2023).

M_2 (Fo50-55): Olivine from M_2 magma can only be generated from an evolved trachyandesite composition under a reduced redox condition QFM-1 (Fig. 6c), and the coexisting liquid with M_2 olivine is trachytic. The crystallizing temperature and pressure ranges of M_2 olivine are 880-1005 ℃, 0.5-1.5 kbar respectively, which is lower than the other olivine population (M_0, M_1, and mm_1). The H_2O content of the melt in equilibrium with this M_2 olivine could range between 0.1-2.5 wt%. Our T-P-H_2O results are comparable to those from Tianchi trachytic pumice (Wang et al. 2025; Chen et al. 2026). Though all

the M_2 olivine were found in trachyandesite enclaves of mingled samples, the M_2 olivine was rather in equilibrium with trachytic melts than with their host trachyandesite (Fig. 7a and b).

M_3 (Fo<5): Magma environment M_3 is represented by one Fe-rich olivine (Fo2.6) in comendite. We did not reproduce it from our initial compositions by MELTS modelling. Alternatively, this crystal is in equilibrium with comendite composition (Fig.7a and b) and its crystallizing temperature was calculated as 855 ℃ by the olivine-liquid geothermometry (Fig. 7c). This result agrees with the temperature range (850-890 ℃) calculated by Chen et al. (2026). Magma environment M_3 associated with the comendite reservoir below Tianchi is generally agreed that it was located at shallow depth (0-2 kbar) with a low fO_2 condition (QFM-2 to QFM) and high H_2O contents in the melt (3-5 wt%) (Horn and Schmincke 2000; Andreeva et al. 2019; Wang et al. 2025; Chen et al. 2026).

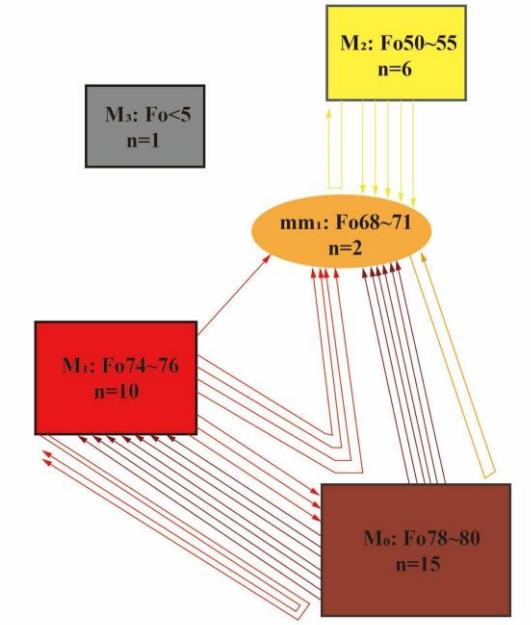


Fig. 8 Systems analysis diagram derived from 34 olivine crystals from our samples. We propose that five magma environments (M_0, M_1, M_2, M_3 and mm_1) identified from olivine populations are represented by boxes and an ellipse. Each box or ellipse is labeled with Fo range and crystal number (n). The connection between different magma environments are depicted by lines with arrows that follow the Fo zoning pathways from crystal interior towards rim (1 olivine crystal only corresponds to 1 arrowed line).

Discussion

1 Interactions between the magmatic environments

The observations from olivine compositions and their zoning patterns suggest multiple open-system interactions between various magmatic environments (M_0, M_1, mm_1, M_2, and M_3). These interactions involve mixing and mingling between different magmas and melts. We have attempted to back-track the olivine pathways using the compositional records from the crystal interiors to the rim following the systems analysis proposed by Kahl et al. (2011). In systems analysis diagrams (Fig. 8), boxes refer to the magma environments, the lines with arrows represent the compositional change trends from the interior to rim of each olivine crystal, among which some complex zoning refers to the pathways involving more than two magma environments.

We found that (1) There is a dominant interaction between two mafic magma environments M_0 and M_1. The interaction marked magma transfer from M_0 to M_1, and recorded by normal zoning M_0-M_1 (7 crystals), reverse zoning M_1-M_0 (3 crystals), and complex zoning M_1-M_0-M_1 (2 crystals). (2) Magma represented by M_0 also intruded into the mm_1 as recorded by the pathway M_0-mm_1 (6 crystals) and mm_1-M_0-mm_1 (1 crystal). (3) The connection between magma environments M_1 and mm_1 includes 2 different pathways. The dominant one is marked by 4 olivine crystals in complex zoning M_1-M_0-mm_1, which give rise to a scenario that the intruding of M_1 magma into mm_1 is powered by a more mafic magma M_0, or there exists some mixing of M_0 magma before M_1-mm_1 intrusion. Direct magma transfer path from M_1 to mm_1 is a minor process only recorded by 1 crystal. (4) Magma environment M_2 represented by low Fo olivine group mainly connects with mm_1 as recorded by pathway M_2-mm_1 (5 crystals) and M_2-mm_1-M_2 (1 crystal). (5) The magma environment represented by the fayalite-rich M_3 related to the comendite magma is not connected to any other reservoirs as the olivine crystal shows a homogeneous profile.

The interactions between M_0, M_1 and mm_1 are most common, representing mafic magma (M_0) intrusions into other magma reservoirs (M_1 and mm_1). The M_1 magma also transfers to mm_1 either through M_0 intrusion pulses or occasionally by direct injection. Moreover, the M_2 magma was apparently not in direct connection with M_0 nor M_1. It only exchanged with intermediate mm_1 magma. Although comendite pumice is observed mingled with other magmas (Fig. 1d and e), we do not find any olivine record of interaction of M_3 (affiliated to comendite magma) with any other magmas. It could be due to the fast injection and cooling of mafic magma into the comendite reservoir and leading subsequent eruption that the olivine crystal has no time to grow.

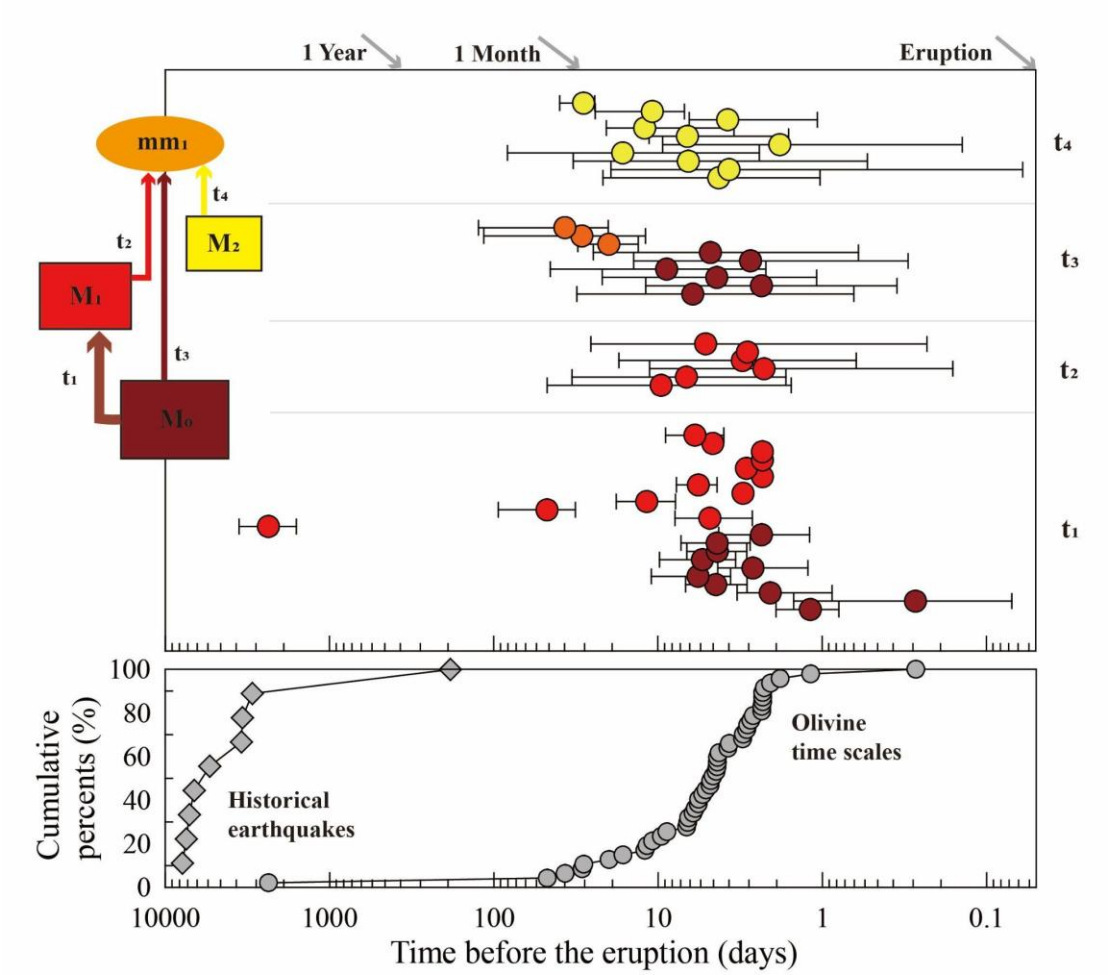


Fig. 9 Time scales of 4 intrusion events derived from diffusion chronometry. Time scale t_1 refers to the time span between M_0-M_1 intrusion and eruption; t_2 refers to the time span between M_1-mm_1 intrusion and eruption; t_3 refers to the time span between intrusion M_0-mm_1 and eruption; t_4 refers to the time span between M_2-mm_1 intrusion and eruption. The error bars on timescales reflect the uncertainties from temperature and analytical precision. The lower panel records the cumulative percentages of diffusion time scales (circles) and historical earthquake events before the Millennium eruption (squares) as discussed in section 4.

2 Time scales constrained from diffusion chronometry

The olivine crystals in our samples are compositionally zoned, which reflects their residence in different magma environments and interactions between them. These zoning features can also record the time scales related to olivine transport through the magma plumbing system before the eruption (Costa and Chakraborty 2004). In this manner we can decipher the time records by modelling the kinetic diffusion of the Fe-Mg (Fo) chemical gradients (Tab. S1 in Supplementary). In total 55 time results were obtained and organized into 4 time spans (t_1, t_2, t_3, and t_4) that refer to the magma intrusion between different reservoirs and residence before eruption (Fig. 9).

The time t_1 is associated with the magma input from environment M_0 to M_1 and includes olivine zoning types of M_0-M_1, M_1-M_0, and M_1-M_0-M_1. We also consider that the first-stage time (Δt_1) from the two-stage modeling of M_1-M_0-mm_1 olivine refers to this process. The time scales of the intrusion events noted as t_1 range between 7 hours to 47 days, with a rare olivine that records a time scale of over 6 years. This process is recorded by the dominant olivine population and thus we suggest that the magma replenishment of M_0 to M_1 is a long-term background process started perhaps as early as 6 years before

the eruption and continued till several hours before the onset of eruption.

Time t_2 relates to subsequent magma migration of M_1 into mm_1, that is represented by two pathways: a major path that the M_1 olivine recharged into mm_1 reservoir carried by deep mafic magma M_0 (stage two of modeling M_1-M_0-mm_1); and a minor path that M_1 olivine recharged directly into mm_1 reservoir (M_1-mm_1). The time scales of these two pathways are noted as t_2, and tend to be shorter than t_1, varying from about 2 and 10 days.

We also found evidence that the mafic magma M_0 intruded directly into mm_1 magma and is recorded by pathways M_0-mm_1 and mm_1-M_0-mm_1. The time scale of this process that we note as t_3 ranges from about 2 to 37 days. The difference of M_0-mm_1 and mm_1-M_0-mm_1 is that M_0-mm_1 denotes the olivine originated in mafic magma M_0 that re-equilibrated its composition with the melts in mm_1 and formed the normal zoning, while mm_1-M_0-mm_1 reflect two events that the mm_1 olivine first influenced by M_0 recharge then separated from the magma mixing zone. The total time related to mm_1-M_0-mm_1 was calculated as $\Delta t_1+\Delta t_2$.

The time span t_4 refers to the duration between magma mm_1 input into M_2 and eruption, which were recorded by olivine M_2-mm_1 and M_2-mm_1-M_2. The modeled time scales of this process range from about 2 days to 28 days.

These results show that the time scales of magma transfer and residence before eruption recorded by the olivine are generally short, with most of them within 1 month. These are much shorter than those obtained from U-Th zircon ages or sanidine results that range hundreds to thousands of years (Zou et al. 2014; Ramos et al. 2019). Such difference in times can be expected as the radiogenic ages likely record the residence or crystallization times rather than the processes that lead to eruption (Costa 2021). Our results are closer to those of olivine diffusion times (about 10 days to 3 years) from Tianchi shield-forming basalts (Tian et al. 2025).

We also note that Shea et al. (2023) propose that the Fe-Mg diffusion coefficient of Dohmen and Chakraborty (2007) and Dohmen et al. (2007) could be up to 10 times slower based on their olivine-melt experiments (though they did not provide the new calibration of $D_{Fe\text{-}Mg}$). If this was the case for the samples we have investigated, it would imply that the time scales of olivine are 10 times shorter, of less than about 3 days. Such time scales seem less realistic for a composite magma plumbing system to activate and erupt, and of a different time frame reported months' period of the recent unrest (Fig. 12 and text in further discussion). Moreover, our samples show crystallization temperatures being <1150 °C, which are plausible for a slower $D_{Fe\text{-}Mg}$ (Oeser et al. 2026; Brückel et al. 2026), thus we have not considered such short times for the overall interpretation.

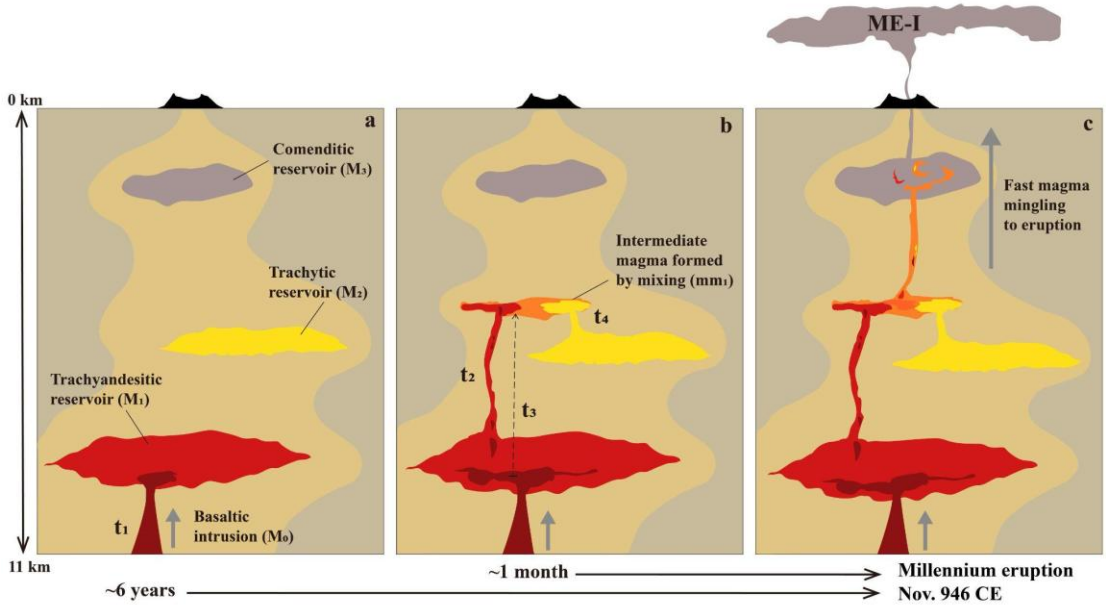


Fig. 10 Proposed Evolutionary model of the magmatic plumbing system and the processes that lead to the Millennium eruption. **a** An early stage of basaltic magma replenishment into trachyandesite reservoir. **b** Interaction between these two mafic magmas and a trachytic reservoir that mixed and led to an intermediate composition of mm_1. **c** Final injection of mixed composition into comendite reservoir and eruption. Note that the size of the magma reservoirs and locations are not to actual scales.

3 The dynamic magma plumbing system and the triggering of Millennium eruption

Using the combined information of field observations, geochemical analysis of melts and whole rocks,

olivine mineralogy, and kinetic diffusion chronometry, we propose the following conceptual model of the shallow plumbing system shortly before and its approach towards the Millennium eruption (Fig. 10).

The magma environments M_0, M_1, mm_1, M_2, and M_3 inferred from the olivine populations were likely physically distinct magma reservoirs that show progressive change of thermodynamic conditions: the temperature and pressure decrease from the hotter (1050-1160 ℃) and deeper (~11 km) mafic reservoirs to felsic ones, accompanied with a decrease on the fO_2 conditions from about NNO to QFM-1. The depth of the magma reservoirs is calculated from the pressure estimation using an average crustal density of 2.7 g/cm^3. The M_0 represents the basalts that provide deep mafic intrusions, whereas magma environments M_1, M_2, M_3 are related to trachyandesite, trachyte, and comendite magma respectively (Fig. 7a and b). Magma environment mm_1 could be an intermediate reservoir that formed by mixing of trachyte and trachyandesite. Previous studies suggest that the Millennium eruption was triggered by the injection of deep mafic melts such as trachyandesite or basalt into the silicic reservoirs (Pan et al. 2017; Kuritani et al. 2020; Wang et al. 2025). While some other studies emphasize the role of mingling between comendite and trachyte before the eruption (Yi et al. 2021; Chen et al. 2026). We did not find an olivine record of the mixing between the comendite and trachyte and thus these two magmas likely simply mingled during the eruption (Pan et al. 2017). The evidence from olivine crystals suggest the following sequence of processes and events before the eruption onset: the deep basaltic magma is the 'engine' to the whole plumbing system, which intruded into trachyandesite reservoir. This process ranges in time scales of years to only several hours (Fig. 10a). Then the trachyandesite was 'activated' and mixed with trachytic magma during ascent, where intermediate reservoir mm_1 was formed (Fig. 10b). Olivine diffusion chronometry shows time scales of days to one month of this process. The final eruption of the volcano was directly triggered by the very fast process that the above-mentioned mixture injected into the comenditic magma chamber (Fig. 10c). This was observed petrologically but was perhaps too fast to be recorded by olivine crystals which are unzoned in Fo.

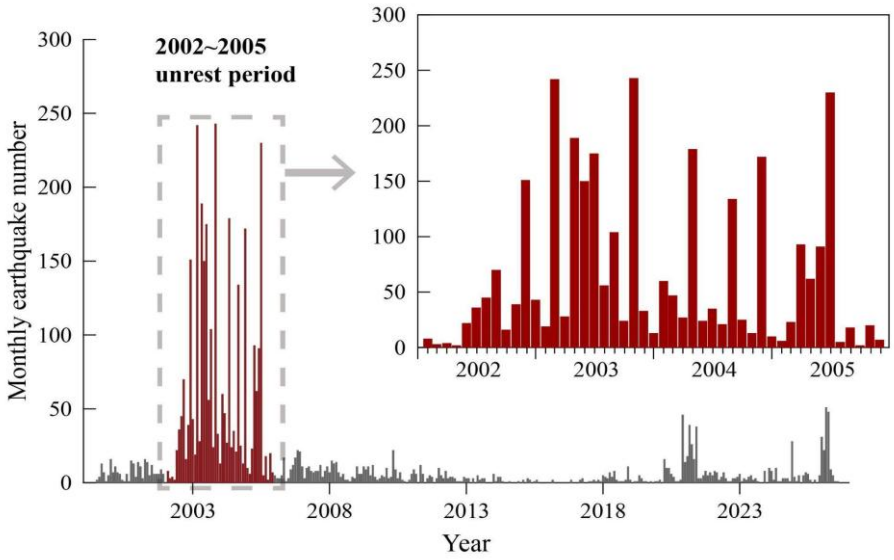


Fig. 11 Monitored earthquake numbers per month from 1998 to 2026. Insert diagram shows the unrest period of Tianchi volcano during 2002-2005. The data source was provided by Changbaishan-Tianchi Volcano Observatory (Xu et al. 2012; Pan et al. 2021; Liu et al. 2026).

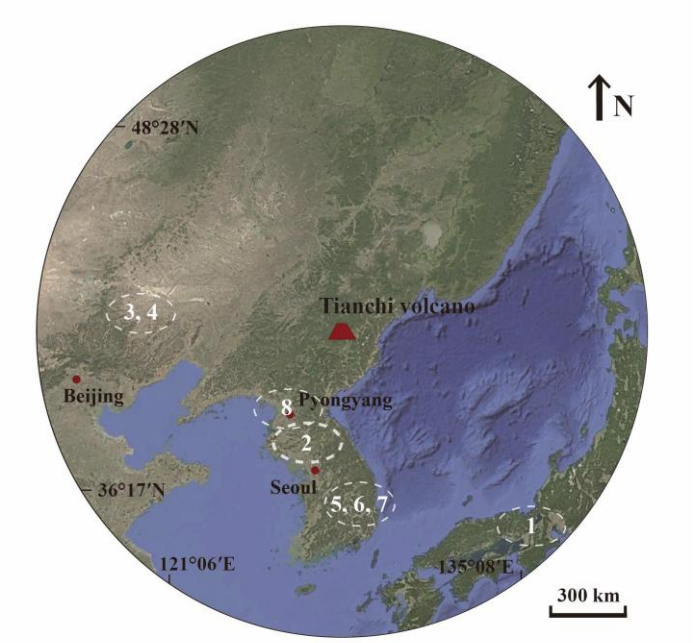


Fig. 12 Estimated locations of historical accounts of earthquakes (white circles) in China, Korea and Japan in the two decades before the Millennium eruption. The numbers in the white circles are corresponding to event numbers in Table 3. The base-map is modified from Google Earth.

Table 3 Historical earthquakes reported in chronicles before the Millennium eruption

	Events	Translation of the original texts	Date	Time scales before the eruption	Estimated location/Distance to the volcano
1	Earthquake	'People died of earthquake and breaking of the ground'	May 3, 946	184 days	Nara, Japan/1057 km
2	Indirect sign	'The withered locust in inner palace rose up by itself'	October, 938	8 years	Kaesong, DPR. Korea/468 km
3	Earthquake	'In Renshen day, earthquake hit the Kaihuang Hall'	July 18, 937	9.3 years	NE China/757 km
4	Earthquake	'In Jiashen day, fourth month, summer, earthquake'	May 31, 937	9.4 years	NE China/757 km
5	Earthquake	'In first month sixth year, spring, earthquake'	March, 932	14.7 years	Gyeongsang-do, R. Korea/691 km
6	Earthquake	'In Jiaxu day, sixth month, earthquake occurred at Bizhen town'	July 29, 928	18.3 years	Gyeongsang-do, R. Korea/676 km
7	Indirect sign	'The pagoda at Hwangnyongsa Temple shook and tilted to the north'	May, 927	19.5 years	Gyeongsang-do, R. Korea/691km
8	Indirect sign	'The bell at a Zen Hall of the Western Capital spontaneously sounded 90 times'	June, 926	20.4 years	Pyongyang, DPR. Korea/381 km

Sources: ***1*** *Kohfukuji Nendaiki (兴福寺年代记). Digital images of the original text. National Archives of Japan, Tokyo.* ***2, 6, 8*** *Goryeosa (高丽史). Digital images of the original text. National Archives of Japan, Tokyo.* ***3, 4*** *Liaoshi (辽史). Digital images of the original text. Harvard-Yenching Library, Cambridge.* ***5, 7*** *Samguk sagi (三国史记). Digital images of the original text. Korean History Database, National Institute of Korean History, Seoul.*

4 Connection to the modern volcanic unrest and historical records

The ground deformation and/or earthquakes caused by magma recharge and mixing are often proposed to be precursors of eruptions. For recent eruptions in well monitored volcanoes it has been possible to link some of the time scales obtained for the processes before the eruption according to the erupted crystals with those of seismic, geodetic and gas unrest signals (Kahl et al. 2011; Rasmussen et al. 2018;

Mourey et al. 2023). For older historical eruptions where there were written records of unrest it has also been possible to integrate the time scales from the crystal zoning with those of the phenomena felt by the population (Albert et al. 2015, 2016). Integration of these various types of information helps in better understanding volcanic monitoring and improve hazard mitigation.

Tianchi volcano has experienced one major episode of volcanic unrest between 2002 and 2005 which included increased seismicity, deformation, and gas releases (Xu et al. 2012). The increase of the volcanic-tectonic earthquakes lasted about 4 years, and included multiple peaks that lasted for about 1-4 months (Fig. 11). These time frames are similar to those we have found for the deep magma intrusion and further interactions from olivine crystals. It could be indicative that the recent unrest between 2002 and 2005 may be related to these processes, as it has already been interpreted from geophysical unrest data by Liu et al. (2026).

At the time of the Millennium eruption it is unclear whether there was a significant population living close to the volcano which could have felt earthquakes or other phenomena before the eruption. Such unrest has been reported by other large Plinian events such as the Pinatubo 1991, and the Minoan eruption (Wolfe and Hoblitt 1999; Druitt et al. 2012), or even smaller and more mafic eruptions in the Canary Islands (Albert et al. 2015). We consulted the written records in history books of ancient China, Korea, and Japan, which includes Liaoshi (辽史. Harvard-Yenching Library), Goryeosa (高丽史. National Archives of Japan), Samguk sagi (三国史记. Korean History Database, National Institute of Korean History), and Kohfukuji Nendaiki (兴福寺年代记. National Archives of Japan). We only identified 8 mentions of earthquake events or other major abnormal phenomena that happened two decades to around 6 months before the onset of the eruption (Fig. 12 and Tab. 3). However, most of these events occurred much earlier than the time scales of magma intrusion that we have calculated (Fig. 9), and their locations are quite far (>300 km) from the volcano. These seismic events were rather regional large tectonic earthquakes than the ones associated with changes of the volcanic system. It thus seems that large earthquakes either were not reported by the people living close to the volcano or not such seismicity occurred. Moreover, the recorded large tectonic earthquakes were both spatially and temporally distant from the eruption, thus were unlikely triggers of the Millennium eruption. Given the apparent lack of relationship between the eruption dates, regional earthquakes, and magma intrusion time scales, it is likely that the magmatic plumbing system evolved towards eruption through the progressive addition of mass and volatiles from depth, leading to progressive pressurization and ultimately failure of the system.

Conclusions

Field and petrological observations show complex magma intrusion and mixing before the Millennium eruption. The olivine compositions and zoning patterns suggest that up to 5 different magmatic environments interacted and were involved in the Millennium eruption: basalts, trachyandesite, intermediate magma, trachyte, and comendite were present in the crustal plumbing system of Tianchi volcano.

Diffusion chronometry on the Fe-Mg zoned olivine revealed that the intrusion of basalts into trachyandesite reservoir could have started up to 6 years before the eruption, and these intrusions were intensified about a month prior to eruption and appear to have continued even in the last few days. The trachyandesite and trachyte reservoirs were activated then formed the intermediate reservoir during the intensification of deep basalts input, with time scales of within one month before eruption.

The close time frames between the petrological records and seismic monitoring data implies that the recent unrest of Tianchi volcano during 2002-2005 points to some similar magmatic processes that also happened before the Millennium eruption. However, there is no historical record of local earthquake activity associated with such volcanic unrest preceding the eruption, while large regional earthquakes occurred mainly decades earlier. Therefore, we propose that the addition of magma and volatile from depth, followed by mixing with variably evolved melts, progressively pressurized the magmatic plumbing system and ultimately triggered the Millennium eruption.

Acknowledgements

This work was supported by the institutional research project of the Institute of Geology, China Earthquake Administration (No. JB-25-03). Bingrui Zhou was supported by the China Scholarship Council (No. 202404190018) during his research stay in France. Field visits by the French team to Changbaishan volcano were supported by the PHC CAI YUANPEI project (No. 52507WK) awarded to Fidel Costa and Jiandong Xu.

We thank Wanqiu Bai and Nicolas Rividi from CNRS, OSU Ecce Terra, Sorbonne Université, for

their assistance with electron microprobe analyses. We are grateful to the Changbaishan-Tianchi Volcano Observatory for providing the seismic monitoring data and to the Mount Changbaishan UNESCO Global Geopark for supporting our field work.

Author contributions

B.Z. designed the study and wrote the original draft. F.C. supervised on methodology and revised the manuscript. B.P. led funding acquisition and instructed on Changbaishan geology. J.X. contributed to the monitoring data.

Declarations

The authors declare no competing interests.

Reference

Albert H, Costa F, Martí J (2015) Timing of magmatic processes and unrest associated with mafic historical monogenetic eruptions in Tenerife island. J Petrol 56:1945–1966. https://doi.org/10.1093/petrology/egv058

Albert H, Costa F, Martí J (2016) Years to weeks of seismic unrest and magmatic intrusions precede monogenetic eruptions. Geology 44:211–214. https://doi.org/10.1130/G37239.1

Andreeva OA, Andreeva IA, Yarmolyuk VV (2019) Effect of redox conditions on the evolution of magmas of Changbaishan Tianchi volcano, China–North Korea. Chem Geol 508:225–233. https://doi.org/10.1016/j.chemgeo.2018.09.039

Andreeva OA, Yarmolyuk VV, Andreeva IA, Borisovskiy SE (2018) Magmatic evolution of Changbaishan Tianchi volcano, China–North Korea: Evidence from mineral-hosted melt and fluid inclusions. Petrology 26:515–545. https://doi.org/10.1134/S0869591118050028

Araya N, Nakamura M, Matsumoto K, Okumura S (2024) Time-resolved trigger processes leading to the Plinian eruptions at Sakurajima volcano, Japan. J Geophys Res Solid Earth 129:e2023JB028558. https://doi.org/10.1029/2023JB028558

Bani P, Normier A, Bacri C, et al (2015) First measurement of the volcanic gas output from Anak Krakatau, Indonesia. J Volcanol Geotherm Res 302:237–241. https://doi.org/10.1016/j.jvolgeores.2015.07.008

Boretti A (2024) Reassessing the cooling that followed the 1991 volcanic eruption of Mt. Pinatubo. J Atmos Sol-Terr Phys 256:106187. https://doi.org/10.1016/j.jastp.2024.106187

Brückel K, Médard E, Costa F, et al (2026) Integrating olivine diffusion chronometry with monitoring data to decipher the magma dynamics at the submarine Fani Maoré volcano. Geochem Geophys Geosystems 27:e2025GC012568. https://doi.org/10.1029/2025GC012568

Chen S, Hou T, Pan R, et al (2026) Multi-level magma reservoir and open system processes of the Tianchi caldera, Changbaishan Volcanic Field, NE China. J Volcanol Geotherm Res 473:108598. https://doi.org/10.1016/j.jvolgeores.2026.108598

Chen X-Y, Blockley SPE, Tarasov PE, et al (2016) Clarifying the distal to proximal tephrochronology of the Millennium (B–Tm) eruption, Changbaishan Volcano, northeast China. Quat Geochronol 33:61–75. https://doi.org/10.1016/j.quageo.2016.02.003

Costa F (2021) Clocks in magmatic rocks. Annu Rev Earth Planet Sci 49:231–252. https://doi.org/10.1146/annurev-earth-080320-060708

Costa F, Chakraborty S (2004) Decadal time gaps between mafic intrusion and silicic eruption obtained from chemical zoning patterns in olivine. Earth Planet Sci Lett 227:517–530. https://doi.org/10.1016/j.epsl.2004.08.011

Costa F, Dohmen R, Chakraborty S (2008) Time scales of magmatic processes from modeling the zoning patterns of crystals. Rev Mineral Geochem 69:545–594. https://doi.org/10.2138/rmg.2008.69.14

Costa F, Shea T, Ubide T (2020) Diffusion chronometry and the timescales of magmatic processes. Nat Rev Earth Environ 1:201–214. https://doi.org/10.1038/s43017-020-0038-x

Dohmen R, Becker H-W, Chakraborty S (2007) Fe–Mg diffusion in olivine I: experimental determination between 700 and 1,200°C as a function of composition, crystal orientation and oxygen fugacity. Phys Chem Miner 34:389–407. https://doi.org/10.1007/s00269-007-0157-7

Dohmen R, Chakraborty S (2007) Fe–Mg diffusion in olivine II: point defect chemistry, change of diffusion mechanisms and a model for calculation of diffusion coefficients in natural olivine. Phys Chem Miner 34:409–430. https://doi.org/10.1007/s00269-007-0158-6

Doronzo DM, Trasatti E, Arienzo I, et al (2023) Magma reservoir growth and ground deformation preceding the 79 CE Plinian eruption of Vesuvius. Commun Earth Environ 4:211. https://doi.org/10.1038/s43247-023-00880-9

Druitt TH, Costa F, Deloule E, et al (2012) Decadal to monthly timescales of magma transfer and reservoir growth at a caldera volcano. Nature 482:77–80. https://doi.org/10.1038/nature10706

Ghiorso MS, Sack RO (1995) Chemical mass transfer in magmatic processes IV. A revised and internally consistent thermodynamic model for the interpolation and extrapolation of liquid-solid equilibria in magmatic systems at elevated temperatures and pressures. Contrib Mineral Petrol 119:197–212

Girona T, Costa F (2013) DIPRA: A user-friendly program to model multi-element diffusion in olivine with applications to timescales of magmatic processes. Geochem Geophys Geosystems 14:422–431. https://doi.org/10.1029/2012GC004427

Giuffrida M, Viccaro M (2017) Three years (2011–2013) of eruptive activity at Mt. Etna: Working modes and timescales of the modern volcano plumbing system from micro-analytical studies of crystals. Earth-Sci Rev 171:289–322. https://doi.org/10.1016/j.earscirev.2017.06.003

Gualda GAR, Ghiorso MS, Lemons RV, Carley TL (2012) Rhyolite-MELTS: a modified calibration of MELTS optimized for silica-rich, fluid-bearing magmatic systems. J Petrol 53:875–890. https://doi.org/10.1093/petrology/egr080

Guo J, Shan X, Yi J, et al (2023) Basaltic magma plumbing system for the cone-construction stage of the Changbaishan from mineralogical, geochemical, and Sr Nd isotopic data. Lithos 448–449:107173. https://doi.org/10.1016/j.lithos.2023.107173

Horn S, Schmincke H-U (2000) Volatile emission during the eruption of Baitoushan Volcano (China/North Korea) ca. 969 AD. Bull Volcanol 61:537–555. https://doi.org/https://doi.org/10.1007/s004450050004

Iacovino K, Ju-Song K, Sisson T, et al (2016) Quantifying gas emissions from the “Millennium Eruption” of Paektu volcano, Democratic People’s Republic of Korea/China. Sci Adv 2:e1600913. https://doi.org/10.1126/sciadv.1600913

Kahl M, Chakraborty S, Costa F, Pompilio M (2011) Dynamic plumbing system beneath volcanoes revealed by kinetic modeling, and the connection to monitoring data: An example from Mt. Etna. Earth Planet Sci Lett 308:11–22. https://doi.org/10.1016/j.epsl.2011.05.008

Kahl M, Chakraborty S, Pompilio M, Costa F (2015) Constraints on the nature and evolution of the magma plumbing system of Mt. Etna volcano (1991–2008) from a combined thermodynamic and kinetic modelling of the compositional record of minerals. J Petrol 56:2025–2068. https://doi.org/10.1093/petrology/egv063

Kuritani T, Nakagawa M, Nishimoto J, et al (2020) Magma plumbing system for the Millennium Eruption at Changbaishan volcano, China: Constraints from whole-rock U–Th disequilibrium. Lithos 366–367:105564. https://doi.org/10.1016/j.lithos.2020.105564

Liu G, Guo Z, Xu J, et al (2026) A critical review of the 2002–2005 volcanic unrest at Changbaishan Volcano, NE China: implications for future volcanic activities. Bull Volcanol 88:63. https://doi.org/10.1007/s00445-026-01981-x

Morgan DJ, Blake S, Rogers NW, et al (2006) Magma chamber recharge at Vesuvius in the century prior to the eruption of A.D. 79. Geology 34:845. https://doi.org/10.1130/G22604.1

Mourey AJ, Shea T, Costa F, et al (2023) Years of magma intrusion primed Kīlauea Volcano (Hawai'i) for the 2018 eruption: evidence from olivine diffusion chronometry and monitoring data. Bull Volcanol 85:18. https://doi.org/10.1007/s00445-023-01633-4

Newhall C, Self S, Robock A (2018) Anticipating future Volcanic Explosivity Index (VEI) 7 eruptions and their chilling impacts. Geosphere 14:572–603. https://doi.org/10.1130/GES01513.1

Oeser M, Dohmen R, Weyer S (2026) Fe-Mg in olivine: simultaneous experimental determination of the diffusion-driven isotope fractionation along with tracer- and inter-diffusion coefficients. Geochim Cosmochim Acta 413:48–66. https://doi.org/10.1016/j.gca.2025.09.036

Oppenheimer C (2011) Eruptions that shook the world. Cambridge University Press, Cambridge, UK

Oppenheimer C, Wacker L, Xu J, et al (2017) Multi-proxy dating the 'Millennium Eruption' of Changbaishan to late 946 CE. Quat Sci Rev 158:164–171. https://doi.org/10.1016/j.quascirev.2016.12.024

Pan B, De Silva SL, Xu J, et al (2020) Late Pleistocene to present day eruptive history of the Changbaishan-Tianchi Volcano, China/DPRK: New field, geochronological and chemical constraints. J Volcanol Geotherm Res 399. https://doi.org/10.1016/j.jvolgeores.2020.106870

Pan B, De Silva SL, Xu J, et al (2017) The VEI-7 Millennium eruption, Changbaishan-Tianchi volcano, China/DPRK: New field, petrological, and chemical constraints on stratigraphy, volcanology, and magma dynamics. J Volcanol Geotherm Res 343:45–59. https://doi.org/10.1016/j.jvolgeores.2017.05.029

Pan B, Liu G, Cheng T, et al (2021) Development and status of active volcano monitoring in China. Geol Soc Lond Spec Publ 510:227–252. https://doi.org/10.1144/SP510-2020-62

Pelullo C, Chakraborty S, Cambeses A, et al (2022) Insights into the temporal evolution of magma plumbing systems from compositional zoning in clinopyroxene crystals from the Agnano-Monte Spina Plinian eruption (Campi Flegrei, Italy). Geochim Cosmochim Acta 328:185–206. https://doi.org/10.1016/j.gca.2022.04.007

Putirka KD (2008) Thermometers and barometers for volcanic systems. Rev Mineral Geochem 69:61–120. https://doi.org/10.2138/rmg.2008.69.3

Ramos FC, Heizler MT, Buettner JE, et al (2016) U-series and 40Ar/39Ar ages of Holocene volcanic rocks at Changbaishan volcano, China. Geology 44:511–514. https://doi.org/10.1130/G37837.1

Ramos FC, Wolff JA, Buettner JE, et al (2019) Ra/Th ages of sanidine in young trachytes erupted at Changbaishan Volcano, China. J Volcanol Geotherm Res 374:226–241. https://doi.org/10.1016/j.jvolgeores.2019.02.006

Rasmussen DJ, Plank TA, Roman DC, et al (2018) When does eruption run-up begin? Multidisciplinary insight from the 1999 eruption of Shishaldin volcano. Earth Planet Sci Lett 486:1–14. https://doi.org/10.1016/j.epsl.2018.01.001

Ribó M, Cronin SJ, Park S-H, et al (2026) Rapid submarine caldera collapse during the 2022 climactic eruption of Hunga volcano (Tonga). Nat Geosci 19:1362–1369. https://doi.org/10.1038/s41561-026-02099-7

Roeder PL, Emslie RF (1970) Olivine-liquid equilibrium. Contrib Mineral Petrol 29:275–289. https://doi.org/10.1007/BF00371276

Romano P, Pelullo C, Chakraborty S, et al (2026) Timescales and magma dynamics of the plumbing system feeding a Plinian eruption: the 79 CE eruption of Somma-Vesuvius, Italy. Geosci Front 17:102283. https://doi.org/10.1016/j.gsf.2026.102283

Shea T, Costa F, Krimer D, Hammer JE (2015) Accuracy of timescales retrieved from diffusion modeling in olivine: A 3D perspective. Am Mineral 100:2026–2042. https://doi.org/10.2138/am-2015-5163

Shea T, Ruth D, Jollands M, et al (2023) The presence of silicate melt may enhance rates of cation diffusion in olivine. Earth Planet Sci Lett 621:118370. https://doi.org/10.1016/j.epsl.2023.118370

Sigurdsson S, Carey S, Cornell W, Pescatore T (1985) The eruption of Vesuvius in AD 79. Natl Geogr Res 1:332–387. https://doi.org/https://digitalcommons.uri.edu/gsofacpubs/1114

Sun C, You H, Liu J, et al (2014) Distribution, geochemistry and age of the Millennium eruptives of Changbaishan volcano, Northeast China — A review. Front Earth Sci 8:216–230. https://doi.org/10.1007/s11707-014-0419-x

Tian Y, Hou T, Wang M, et al (2025) The transition of the magma plumbing system of Tianchi shield-forming basalts, Changbaishan Volcanic Field, NE China: Constraints from dynamic Fe-Mg diffusion modeling in olivine. Am Mineral 110:65–81. https://doi.org/10.2138/am-2023-9296

Wang D-B, Liu P-P, Wei H, et al (2025) Micro-Analytical Perspectives on the Trans-Crustal Magma Plumbing System Feeding the Millennium Eruption of the Tianchi Volcano in the Changbaishan Volcanic Field, Northeast China. J Petrol 66:7. https://doi.org/10.1093/petrology/egaf058

Wolfe EM, Hoblitt RP (1999) Overview of the Eruptions. In: Fire Mud. https://pubs.usgs.gov/pinatubo/wolfe/. Accessed 8 Nov 2026

Xu J, Liu G, Wu J, et al (2012) Recent unrest of Changbaishan volcano, northeast China: A precursor of a future eruption? Geophys Res Lett 39:16. https://doi.org/10.1029/2012GL052600

Xu J, Pan B, Liu T, et al (2013) Climatic impact of the Millennium eruption of Changbaishan volcano in China: New insights from high-precision radiocarbon wiggle-match dating. Geophys Res Lett 40:54–59. https://doi.org/10.1029/2012GL054246

Yang Q, Jenkins SF, Lerner GA, et al (2021) The Millennium Eruption of Changbaishan Tianchi Volcano is VEI 6, not 7. Bull Volcanol 83:74. https://doi.org/10.1007/s00445-021-01487-8

Yeo NE, Choi SH, Yu Y, Kim J-I (2026) Lithology and redox–hydration state of the mantle source of the late Cenozoic Baekdusan (Changbaishan) basalts, North China Craton. J Asian Earth Sci 302:107017. https://doi.org/10.1016/j.jseaes.2026.107017

Yi J, Wang P, Shan X, et al (2021) Modeling the multi-level plumbing system of the Changbaishan caldera from geochemical, mineralogical, Sr-Nd isotopic and integrated geophysical data. Geosci Front 12:101171. https://doi.org/10.1016/j.gsf.2021.101171

Zhang M, Guo Z, Liu J, et al (2018) The intraplate Changbaishan volcanic field (China/North Korea): A review on eruptive history, magma genesis, geodynamic significance, recent dynamics and potential hazards. Earth-Sci Rev 187:19–52. https://doi.org/10.1016/j.earscirev.2018.07.011

Zou H, Fan Q, Yao Y (2008) U–Th systematics of dispersed young volcanoes in NE China: Asthenosphere upwelling caused by piling up and upward thickening of stagnant Pacific slab. Chem Geol 255:134–142. https://doi.org/10.1016/j.chemgeo.2008.06.022

Zou H, Fan Q, Zhang H, Schmitt AK (2014) U-series zircon age constraints on the plumbing system and magma residence times of the Changbai volcano, China/North Korea border. Lithos 200–201:169–180. https://doi.org/10.1016/j.lithos.2014.04.020

Supplementary Files

This is a list of supplementary files associated with this preprint. Click to download.

- Supplementary.docx